Interatomic potentials for strontium titanate: An assessment of their transferability and comparison with density functional theory

Nicole A. Benedek,[1,2,*] Alvin L.-S. Chua,[2] Christian Elsässer,[3] Adrian P. Sutton,[2] and Mike W. Finnis[1,2]
[1]*Department of Materials, Imperial College London, Exhibition Road, London SW7 2AZ, United Kingdom*
[2]*Department of Physics, Imperial College London, Exhibition Road, London SW7 2AZ, United Kingdom*
[3]*Fraunhofer Institut für Werkstoffmechanik, Wöhlerstraße 11, 79108 Freiburg, Germany*
(Received 12 May 2008; published 13 August 2008)

The technological importance of polycrystalline strontium titanate ($SrTiO_3$) is directly linked to its interfacial and grain boundary properties, which are at present poorly understood. A complete understanding (including links with experiment) requires information from many length scales, including electronic and atomistic, up to microstructural and macroscopic. In addition, the size and complexity of many general grain boundaries makes first-principles simulations prohibitively expensive. We have tested the ability of a number of interatomic potentials from the literature to accurately describe at least the structures of some simple grain boundaries in $SrTiO_3$. The potentials we have tested are of three types: rigid ion model with either fixed formal or partial charges and shell model. We have also performed a detailed density functional theory (DFT) study of the same boundaries and used this data (interface structures and energies) to validate the interatomic potentials. Our conclusion is that none of the potentials can reproduce the energy ordering of the boundaries predicted by the DFT calculations. The boundary structures produced by some of the potentials do however agree reasonably well with the DFT structures. We discuss the implications of our findings for ionic oxide grain boundary research and critically examine the rigid ion and shell model approximations.

DOI: 10.1103/PhysRevB.78.064110 PACS number(s): 61.72.Mm, 68.35.−p

I. INTRODUCTION

Computer simulations are playing a vital role in furthering our understanding of grain boundary (GB) structure and properties. Classical simulations have been used extensively in investigations of the structure of tilt boundaries in pure cubic metals.[1] More recently, classical molecular dynamics studies have clarified the role of grain boundaries in the deformation mechanisms of nanocrystalline metals.[2] A recent computational study of twist boundaries in silicon showed that the lowest energy boundaries could only be accessed by removing atoms from within a slab of finite width centered on the GB.[3] The resulting configurations were used as the starting points for long (60 ns) molecular dynamics simulations. The long-range nature of the Coulomb interaction makes such large-scale simulations of intefaces in ionic materials more time-consuming and in the early days of scientfic computing, this was a serious impediment to the study of ionic interfaces. However, increases in computer power and improved algorithms mean this is no longer such a problem. Ionic materials contain at least two different species of atom and this *does* introduce additional complications. For example, in any multicomponent system interfacial free energies are a function of the chemical potentials of the constituents, as manifest in the Gibbs adsorption equation. The stoichiometry of the interface, described by interfacial excess quantities, should therefore be varied to minimize the interfacial free energy. Furthermore, if the simulations are being performed with periodic boundary conditions, any charged point defects that are present will interact with an infinite array of images of themselves, as well as with a compensating background; this will affect the interfacial energy. Hence, computer simulations of ionic interfaces are usually limited to relatively simple, defect-free boundaries with small periodic cells and consequently, less is known about grain boundaries in ionic materials than in metals.

In this paper, we present a detailed atomistic study of the SrO_3-terminated $\Sigma 3(111)[\bar{1}10]$ and SrTiO-terminated $\Sigma 3(112)[\bar{1}10]$ symmetrical tilt grain boundaries (STGB) in $SrTiO_3$. $SrTiO_3$ is a technologically important perovskite electroceramic. For example, in addition to being used as a barrier layer capacitor, it is also a candidate for use in high-density electronic memory applications[4] and shows promise as a potential thermoelectric material.[5] The bulk properties of $SrTiO_3$ are generally well understood, however the same cannot be said of $SrTiO_3$ grain boundaries. In the present work, only stoichiometric boundaries have been studied, that is, boundaries with no excess of any of the three components (Sr, Ti, or O).

The Si twist boundary simulations described above are currently only feasible with interatomic potentials. Before we can perform such simulations for grain boundaries in $SrTiO_3$, we must first identify a suitable interatomic potential. The purpose of this investigation is therefore to test the available interatomic potentials for $SrTiO_3$ on some relatively simple grain boundaries and to compare the results to first-principles density functional theory (DFT) calculations. We have calculated the relaxed structures and energies of the chosen interfaces and located stable translation states by exploring the γ surface.[6] In order to keep the *ab initio* simulations manageable, we have chosen periodic boundaries with small unit cells. There have been several previous studies, both experimental[7,8] and theoretical,[9–11] on the $\Sigma 3(111)[\bar{1}10]$ STGB and one experimental study of the $\Sigma(112)[\bar{1}10]$ system.[12]

Throughout this work we will implicitly assume that the DFT in the local density approximation (LDA) reliably gives

 ©2008 The American Physical Society

accurate grain boundary energies. The success of DFT in material modeling suggests that this is a very reasonable assumption. However, there have been no high-level calculations [Quantum Monte Carlo (QMC), for example] on grain boundaries; hence we have no guarantee that the commonly used DFT approximations [LDA and generalized gradient approximation (GGA)] will not produce systematic errors in the grain boundary energies. Alfé and Gillan[13] recently performed a series of QMC calculations on the (001) surface of MgO. Their results showed that the QMC and LDA energies were in good agreement but that the GGA energy was too low by ~30% [the apparently superior performance of the LDA is thought to be due to a more favorable cancellation of errors than in the GGA (Ref. 14); there has been recent progress on the surface energy problem for GGAs (Refs. 15 and 16)]. There have been no such studies assessing the performance of DFT for grain boundary energies. The changes in atomic coordination at a grain boundary are less abrupt than at a surface, hence grain boundary energies should not be in error (if they are in error at all) as much as GGA surface energies. However, researchers should be aware of the possibility of DFT errors when comparing the results of DFT and interatomic potential calculations of grain boundaries, particularly when there are large local changes in the coordination of ions.

This paper is organized as follows. In Sec. II, we describe our computational methods, starting with a brief review of the classical models used in this work. The structures of the grain boundaries we are investigating are described in Sec. II C and one of the candidate interatomic potentials is used to compute the γ surface for the $\Sigma 3(112)$ GB. We present DFT results on the structures and energetics of the boundaries in Sec. III A and results for the classical models in Sec. III B. We compare our findings to those of other authors in Sec. IV and we conclude in Sec. V.

II. CALCULATIONS

A. Classical potentials

Perhaps the most widely used classical model of interatomic forces in ionic materials is the modified Buckingham potential,

$$U_{ij} = A \exp(-r_{ij}/\rho) - \frac{C_6}{r_{ij}^6} + \frac{q_i q_j}{r_{ij}}, \tag{1}$$

where A, ρ, and C_6 are parameters to be fitted. The exponential term on the right-hand side of the equation is short ranged and represents repulsive overlap interactions between pairs of ions. The second term is longer ranged and represents attractive van der Waals interactions between the ions. These first two terms together constitute the Buckingham potential. The third term is the Coulomb interaction between pairs of ions of charge q (fixed formal charges are assumed).

The simplest way to improve the Buckingham picture of rigid ions is to include terms which describe the polarizability of the ions. The earliest approach is provided by the shell model of Dick and Overhauser,[17] in which an atom is represented as a core attached to a massless shell of charge q_s by a harmonic spring. The core represents the nucleus of the atom plus all the inner electrons while the shell represents the outer or valence electrons. The sum of the core and shell charges is equal to the formal charge on the ion. The free-atom polarizability α is thus given by:

$$\alpha = \frac{q_s^2}{k}, \tag{2}$$

where k is the spring constant. Both the shell charge and the spring constant are empirical parameters. The shells repel each other through the short-range interaction while the Coulomb interaction acts on both cores and shells.

The shell model can be further improved by allowing the radius of the shells to vary in response to their environment, as in the breathing shell model[18] or the more recent compressible ion model (CIM) of Pyper *et al.*[19,20] The compressibility of an ion has a significant effect on its properties; this is particularly true of the O^{2-} ion, which is unstable in free space. The aspherical ion model (AIM) of Madden and coworkers[21] also takes account of dipole polarizability and ion compressibility, as in the shell and compressible ion models. In addition, the AIM includes terms which describe the quadrupole polarizability of the ions.

While the functional forms and parameters of the above polarizable ion models are mostly empirical, the general concepts can be derived from density functional theory, via a tight-binding representation of the electronic structure.[22] Tight binding can incorporate in a physically based model the concepts of polarization and charge transfer, besides the Coulomb interaction. The difficulty, both in tight binding and its derivative classical models, lies in the fitting of functions and parameters to experimental or computed data, and the subsequent all-too-common discovery that an empirical model may not be as transferable as its authors hoped. This leads to the common situation that several potentials are available in the literature for most common materials.

None of the potentials we have selected for testing were fitted to grain boundary structures or properties. Akhtar *et al.*[23] used a modified Buckingham potential in combination with the shell model to investigate the relationship between electrical properties and defect structures in doped and undoped bulk $SrTiO_3$. McCoy *et al.*[24] also used the Buckingham and shell models in their study on the stability of the Ruddlesden-Popper shear phases in $SrTiO_3$. Crawford and Jacobs[25] used a modified Buckingham potential to calculate the solubility of various impurity ions in $SrTiO_3$. Thomas *et al.*[26] developed a simple pair potential for simulating radiation damage in complex oxides. It is a partial charge model, which consists only of a Born-Mayer repulsion term and a Coulomb term. The partial charges were derived from a Mulliken population analysis from *ab initio* calculations of bulk $SrTiO_3$.

The accurate description of the structures and energetics of our chosen grain boundaries will provide a demanding test of transferability for these potentials.

All of our classical simulations have been performed with the GULP (Ref. 27) package. We used the published cutoff radius for each potential, in combination with a tapering

function (fifth order polynomial), which was applied 1–2 Å before the cutoff. The tapering function ensures that the potential goes smoothly to zero, thereby eliminating discontinuities in the energy and its derivatives. Although the authors of the potentials described above did not apply tapering functions in their work, we found that doing so made the simulations considerably more stable (faster convergence in structural optimizations and smaller forces on the final, relaxed structure). Table I lists the parameters for each potential considered in this work.

B. First-principles calculations

Our first-principles calculations have been performed within the LDA to DFT as implemented in the CASTEP package.[28] Ionic cores were represented by the ultrasoft pseudopotentials provided with the CASTEP distribution. The explicitly treated valence states were $(3s^2,3p^6,3d^2,4s^2)$ for Ti, $(4s,4p,5s)$ for Sr, and $(2s,2p)$ for O. For comparison, we also performed a second set of DFT-LDA calculations with the mixed-basis pseudopotential (MBPP) code of Refs. 29 and 30. Norm-conserving pseudopotentials were used for the ionic cores. The explicitly treated valence states and the **k**-point mesh were the same as with CASTEP. A mixed basis of plane waves up to a cutoff energy of 340 eV plus a set of atom-centered orbitals for the stronger localized semicore and valence states were used. Further technical details can be found in Refs. 9 and 31.

The grain boundary energy and free volume expansion for both the $\Sigma 3(111)[\bar{1}10]$ and $\Sigma(112)[\bar{1}10]$ STGBs were found to be converged with a plane wave cutoff of 500 eV and a $4\times4\times1$ Monkhorst-Pack mesh. We performed a full optimization of the internal coordinates for each grain boundary using the Broyden-Fletcher-Goldfarb-Shanno algorithm and a force convergence tolerance of 0.05 eV/Å. We also optimized the length of the c axis (which is perpendicular to the interface in our models) while keeping the a and b axes fixed at their theoretical lengths.

The grain boundary energy, σ_{GB}, for a stoichiometric interface is defined as

$$\sigma_{GB} = \frac{E_{GB} - E_{bulk}}{2A}, \tag{3}$$

where E_{GB} and E_{bulk} are the total energies of the grain boundary and bulk supercells respectively, and A is the area of the interface; the factor of 1/2 is needed to account for the presence of two symmetrically equivalent grain boundaries per simulation cell (all of our simulations are performed in periodic boundary conditions). The bulk supercells had the same physical dimensions and number of atoms as the grain-boundary-containing cells and their energies were calculated with the same plane wave cutoff and **k**-point sampling. Table II shows the physical dimensions and grain boundary separation for each supercell we investigated.

C. Grain boundary structures: Exploring the γ surface

One grain can be rigidly displaced relative to the other in directions parallel to the interface. Such an operation is known as a rigid body translation $\boldsymbol{t}$. We wish to locate all the metastable energy minima, which we need for comparison of different potentials, besides locating the global minimum energy for a given model. Stable configurations can be initially located either by visual inspection (one may be able to identify mirror or mirror-glide planes by examining the symmetry properties of the boundary) or computationally, by exploring the γ surface, which gives the grain boundary energy

TABLE I. Interatomic potential parameters for the models being tested in this work. All the models assume fixed formal charges on the ions, except for the Thomas potential, which assumes fixed partial charges. A dash in any column indicates that that particular term is zero (absent) for the potential. Note that there is an error in the value of ρ for the O^{2-}-O^{2-} interaction of the McCoy potential as originally published in Ref. 24. We reproduce the correct value here.

Interaction	A (eV)	ρ (Å)	C (eVÅ^{-6})
Buckingham Potentials			
		Akhtar	
Sr^{2+}–O^{2-}	776.84	0.35867	
Ti^{4+}–O^{2-}	877.20	0.38096	9.0
O^{2-}–O^{2-}	22764.3	0.1490	43.0
		McCoy	
Sr^{2+}–O^{2-}	682.172	0.39450	
Ti^{4+}–O^{2-}	2179.122	0.30384	8.986
O^{2-}–O^{2-}	9547.960	0.21916	32.00
		Crawford	
Sr^{2+}–Sr^{2+}	9949.1	0.2446	
Sr^{2+}–Ti^{4+}	12708.1	0.2191	
Sr^{2+}–O^{2-}	1805.2	0.3250	
Ti^{4+}–Ti^{4+}	16963.1	0.1847	
Ti^{4+}–O^{2-}	854.0	0.3770	
O^{2-}–O^{2-}	22764.3	0.1490	20.37
		Thomas	
$Sr^{1.84+}$–$O^{1.40-}$	1769.51	0.319894	
$Ti^{2.36+}$–$O^{1.40-}$	14567.4	0.197584	
$O^{1.40-}$–$O^{1.40-}$	6249.17	0.231472	
Shell Models			
Species	q_s ($\|e\|$)	k (eVÅ^{-2})	
		Akhtar	
Sr^{2+}	1.526	11.406	
Ti^{4+}	−35.863	65974.0	
O^{2-}	−2.389	18.41	
		McCoy	
Ti^{4+}	−0.1	200	
O^{2-}	−2.04	6.3	
		Crawford	
Sr^{2+}	7.468	421.9	
Ti^{4+}	−35.863	30490.0	
O^{2-}	−2.249	24.9	

TABLE II. Simulation cell dimensions and grain boundary separations. The theoretical lattice constant for bulk $SrTiO_3$ is given by a_0=3.857 Å (DFT-LDA).

Number of atoms	Axes (a, b, c)	Dimensions ($\|a\|$, $\|b\|$, $\|c\|$)	Grain boundary separation (Å)
$\Sigma 3(111)[\bar{1}10]$			
60	$[11\bar{2}],[\bar{1}10],[111]$	$\sqrt{6}a_0,\sqrt{2}a_0,2\times\sqrt{3}a_0$	6.68
120		$\sqrt{6}a_0,\sqrt{2}a_0,4\times\sqrt{3}a_0$	13.36
$\Sigma(112)[\bar{1}10]$			
60	$[11\bar{1}],[\bar{1}10],[112]$	$\sqrt{3}a_0,\sqrt{2}a_0,2\times\sqrt{6}a_0$	9.45
120		$\sqrt{3}a_0,\sqrt{2}a_0,4\times\sqrt{6}a_0$	18.89

at each translation $\boldsymbol{t}$.[6] The γ surface is constructed by choosing a particular translation vector parallel to the boundary and then constraining each atom so that it may move only perpendicular to the interface. The a- and b-cell lengths remain fixed throughout the simulation, while the c-cell length is systematically enlarged in small increments. The energy is calculated for each c-cell length and the lowest-energy structure becomes a data point on the γ surface. While the grain boundary energy so calculated has no physical significance, the structure provides a useful starting point for an unconstrained relaxation, during which the translations and atomic positions are all free.

We have calculated the γ surface for both the $\Sigma 3(111)[\bar{1}10]$ and $\Sigma 3(112)[\bar{1}10]$ STGBs using the ionic part of the Akhtar potential (the shells are "frozen" to their cores). Our results for the $\Sigma 3(111)[\bar{1}10]$ boundary agree with previous experimental[7] and theoretical[9] studies in that the most stable state is mirror symmetric, which we define as $\boldsymbol{t}=(0,0)[11\bar{2}],[\bar{1}10]$. In the discussion that follows we will therefore only consider results for the $\Sigma(112)[\bar{1}10]$ STGB.

Figure 1 shows the γ surface for the $\Sigma 3(112)[\bar{1}10]$ grain boundary. There is a trough of low-energy states present between $\sim\boldsymbol{t}=(-1/5,0)$ and $\boldsymbol{t}=(0,0)$. The dots and triangles

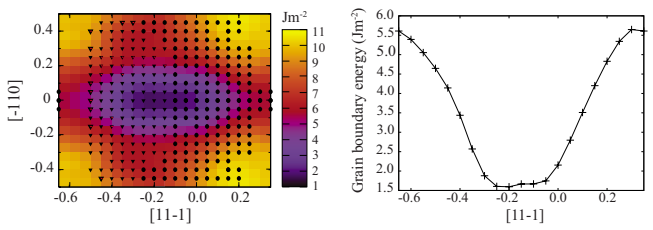

FIG. 1. (Color online) The γ surface for the $\Sigma 3(112)[\bar{1}10]$ grain boundary (left). The x and y axes represent translations along $[11\bar{1}]$ and $[\bar{1}10]$, respectively, in units of the length of the $[\bar{1}10]$ and $[11\bar{1}]$ vectors. The energies plotted are the grain boundary energies of the translation states, with darker colors representing lower-energy interfaces. The meaning of the data represented by the solid black dots and triangles is explained in the text. The variation of the grain boundary energy with the x coordinate fixed at $[\bar{1}10]$=0 is shown in the right-hand-side image.

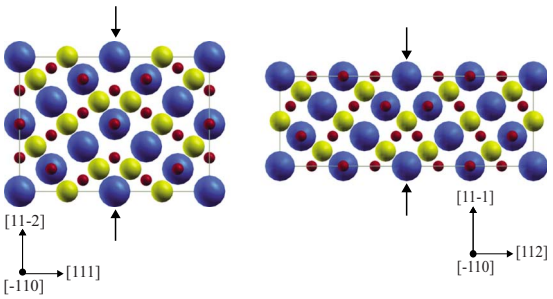

FIG. 2. (Color online) Unrelaxed structures of the $\Sigma 3(111)$ (left) and $\Sigma 3(112)(0,0)$ (right) grain boundaries. The arrows indicate the position of the grain boundary in each model. Blue spheres represent Sr ions, yellow spheres represent Ti ions, and red spheres represent O ions.

superimposed on the γ surface represent simulation cells where the atomic constraints have been released, i.e., the atoms are freed to move in the x, y, and z directions. The dots represent structures which were constructed in the particular translation state shown on the plot and then "slide into" the mirror-symmetric $\boldsymbol{t}=(0,0)$ state upon atomic relaxation. The triangles represent structures which slide into a $\boldsymbol{t}=(2a_0)/3[11\bar{1}]$ state upon atomic relaxation (the $2/3[11\bar{1}]$ state is equivalent to the $-1/3[11\bar{1}]$ state shown in Fig. 1). Hence, when the constraints are released there is no longer a series of low-energy states around $\boldsymbol{t}=(0,0)$, but two distinct minima at $\boldsymbol{t}=(0,0)$ and $\boldsymbol{t}=(2a_0)/3[11\bar{1}]$. This indicates that atomic relaxations parallel to the interface are as important as those perpendicular to the interface.

We therefore have three candidate structures on which to test the interatomic potentials: the SrO_3-terminated $\Sigma 3(111)[\bar{1}10]$ grain boundary and the SrTiO-terminated $\Sigma 3(112)[\bar{1}10](0,0)$ and O_2-terminated $\Sigma 3(112)[\bar{1}10](2/3,0)$ boundaries. Since the tilt axis is $[\bar{1}10]$ for all three boundaries, we will refer to the $\Sigma 3(111)[\bar{1}10]$ GB as simply the $\Sigma 3(111)$ boundary and the two $\Sigma 3(112)$ boundaries as $\Sigma 3(112)(0,0)$ and $\Sigma 3(112)(2/3,0)$. The $\Sigma 3(111)$ and $\Sigma 3(112)(0,0)$ boundaries both have mirror-symmetry, while the $\Sigma 3(112)(2/3,0)$ has mirror-glide symmetry. The structures of the grain boundaries are shown in Figs. 2 and 3. Figure 4 shows the relationship between the $\Sigma 3(112)(0,0)$ and $\Sigma 3(112)(2/3,0)$ grain boundaries.

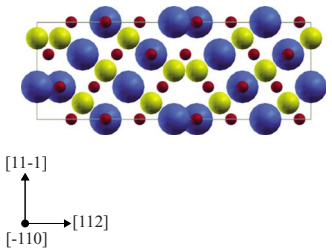

FIG. 3. (Color online) Unrelaxed structure of the $\Sigma 3(112)(2/3)$ GB. The atomic coloring scheme is the same as that for Fig. 2.

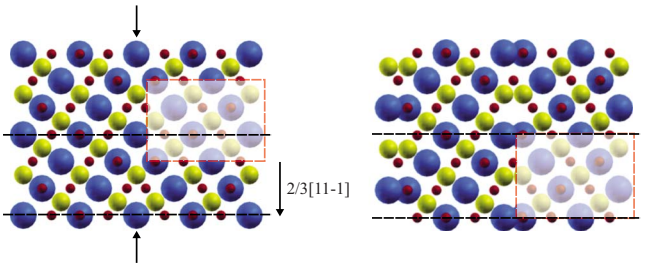

FIG. 4. (Color online) Creation of the $\Sigma 3(112)(2/3,0)$ boundary (right) by a translation of $2/3[11\bar{1}]$ from the $\Sigma 3(112)(0,0)$ boundary (left). The arrows on the left image indicate the position of the GB, which is a mirror plane. The structure on the right is created by shifting all material to the right of the arrows (the GB plane is held fixed) by $2/3[11\bar{1}]$. The resulting structure, the $\Sigma 3(112)(2/3,0)$ boundary, has mirror-glide symmetry about the O_2 GB plane; the glide distance is $1/2[\bar{1}10]$. Both grain boundaries are shown as $2\times1\times1$ supercells. The shaded boxes with red borders represent the same area of crystal for both structures. The black dashed lines represent the borders of the simulation cell for each boundary.

III. RESULTS

A. First -principles calculations

The creation of an unrelaxed grain boundary from truncated crystal lattices will often bring atoms very close together at the interface. The boundary expansion is a response to the strong repulsion between these atoms (the expansion is defined as the excess volume of the boundary per unit area; it can also be thought of as the component of $\boldsymbol{t}$ perpendicular to the interface). Our calculated values of the expansion and energy for the $\Sigma 3(111)$ boundary (Table III) are in good agreement with those of previous DFT calculations.[9–11] They are also in good agreement with the recent high-resolution transmission electron microscopy (HRTEM) experiments of Zhang *et al.*,[8] who found that the interplanar spacing of the planes immediately adjacent to the grain boundary was increased relative to the bulk value.

Figure 5 shows how the interplanar spacing varies as a function of distance from the interface for 60- and 120-atom models of a relaxed $\Sigma 3(111)$ boundary. The deviation from the bulk (111) interplanar spacing Δd_{ij} between adjacent planes i and j is defined as

TABLE III. Relaxed grain boundary energies and expansions from first-principles calculations (DFT-LDA) with CASTEP (energies calculated with MBPP in parentheses for comparison).

Boundary	Number of atoms	Expansion (Å)	Energy (Jm^{-2})
$\Sigma 3(111)$	60	0.13	0.53 (0.52)
	120	0.17	0.57 (0.57)
$\Sigma 3(112)$	60	0.14	1.06 (1.07)
	120	0.19	1.10
$\Sigma 3(112)(2/3,0)$	60	0.43	1.06 (1.04)
	120	0.43	1.10

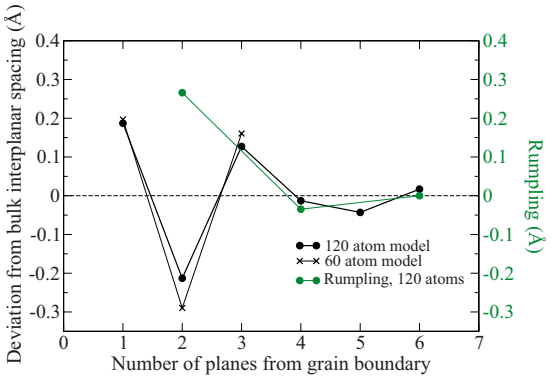

FIG. 5. (Color online) Deviations from the bulk (111) interplanar spacing and variation in rumpling for a relaxed $\Sigma 3(111)$ grain boundary from DFT-LDA calculations. The black circles and green (gray) circles represent interplanar spacing and rumpling data, respectively, for the 120-atom model. The black crosses represent interplanar spacing data for the 60-atom model. The dashed line at $y=0$ is a guide to the eye.

$$\Delta d_{ij} = |[(\mathrm{Sr}_j^z + \mathrm{O}_j^z)/2] - \mathrm{Ti}_i^z| - d_{\mathrm{bulk}}. \quad (4)$$

The terms Sr^z, Ti^z, and O^z denote the relaxed z coordinates of the Sr, Ti, and O atoms, respectively, and d_{bulk} is the interplanar spacing between (111) planes in bulk $SrTiO_3$ from DFT-LDA calculations. The SrO term in square brackets really denotes the *average* relaxed coordinates of the relevant atoms because the SrO layers rumple, i.e., the displacements of the Sr and O atoms along z are not equivalent. The rumpling (also plotted in Fig. 5) of the ith SrO layer η_i is defined as

$$\eta_i = \mathrm{Sr}_i^z - \mathrm{O}_i^z. \quad (5)$$

We have used the notation of Ref. 32 in defining Δd and η.

Figure 5 shows that the interplanar spacing oscillates about its bulk value and converges about four planes from the boundary for the 120-atom model. Both the 60- and 120-atom models show a similar relaxation pattern, which suggests that finite size effects on the atomic relaxations are small. Also shown in Fig. 5 is the rumpling of the SrO layers for the 120-atom model, which is greatest close to the boundary before decaying very quickly to its bulk value.

Deviations from the bulk (112) interplanar spacing and rumpling for the $\Sigma 3(112)(0,0)$ boundary are shown in Fig. 6. Again, the interplanar spacing oscillates about its bulk value but this time, the amplitudes of the oscillations are larger close to the boundary and they decay much more slowly in comparison to the $\Sigma 3(111)$ boundary. The boundary energy, 1.06 J m^{-2}, is significantly higher than that of the $\Sigma 3(111)$ GB. Ideally, one would like to find some relationship between the boundary energy and expansion and perhaps relate changes in these parameters to properties of the constituent grains, such as the interplanar spacing. However, for boundaries with periodicity in the boundary plane (such as the ones we are studying), it is not possible to simply correlate the energy with the expansion because these quantities are complicated functions of many variables: the translation state $\boldsymbol{t}$, the presence of directional bonding, and

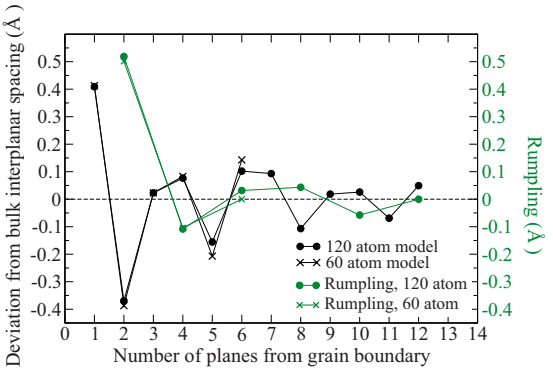

FIG. 6. (Color online) Deviations from the bulk (112) interplanar spacing and variation in rumpling for a relaxed $\Sigma 3(112)(0,0)$ mirror symmetric grain boundary from DFT-LDA calculations. The black circles and green (gray) circles represent interplanar spacing and rumpling data, respectively, for the 120-atom model. The black and green (gray) crosses represent interplanar spacing and rumpling data for the 60-atom model, respectively. The dashed line at $y=0$ is a guide to the eye.

for ionic systems, electrostatic interactions between the constituent ions. The reader is referred to Refs. 33 and 34 for more information.

Finally, we consider the results for the $\Sigma 3(112)(2/3,0)$ GB, which are shown in Fig. 7. The magnitude of both the rumpling and the deviation from the bulk interplanar spacing close to the interface is smallest for the $\Sigma 3(112)(2/3,0)$ boundary compared to the previous two. This probably stems from the mirror-glide symmetry of the $\Sigma 3(112)(2/3,0)$ GB, which results in like-charged ions on opposite sides of the interface having a staggered configuration. This is in contrast to the $\Sigma 3(112)(0,0)$ and $\Sigma 3(111)$ GBs, where the mirror-symmetry of the boundary forces like-charged ions to be directly opposite each other, thereby increasing the repulsion between them and increasing the rumpling and interplanar spacing oscillations.

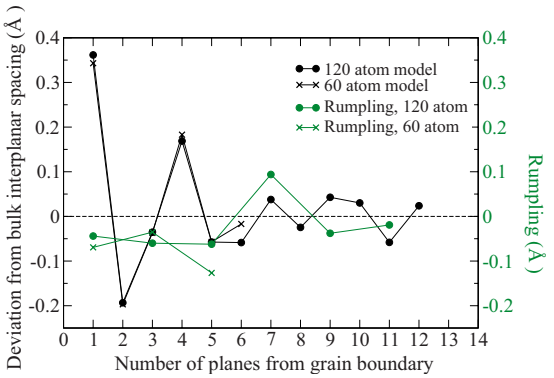

FIG. 7. (Color online) Deviations from the bulk (112) interplanar spacing and variation in rumpling for a relaxed $\Sigma 3(112)(-1/3,0)$ grain boundary from DFT-LDA calculations. The black circles and green (gray) circles represent interplanar spacing and rumpling data, respectively, for the 120-atom model. The black and green (gray) crosses represent interplanar spacing and rumpling data for the 60-atom model, respectively. The dashed line at $y=0$ is a guide to the eye.

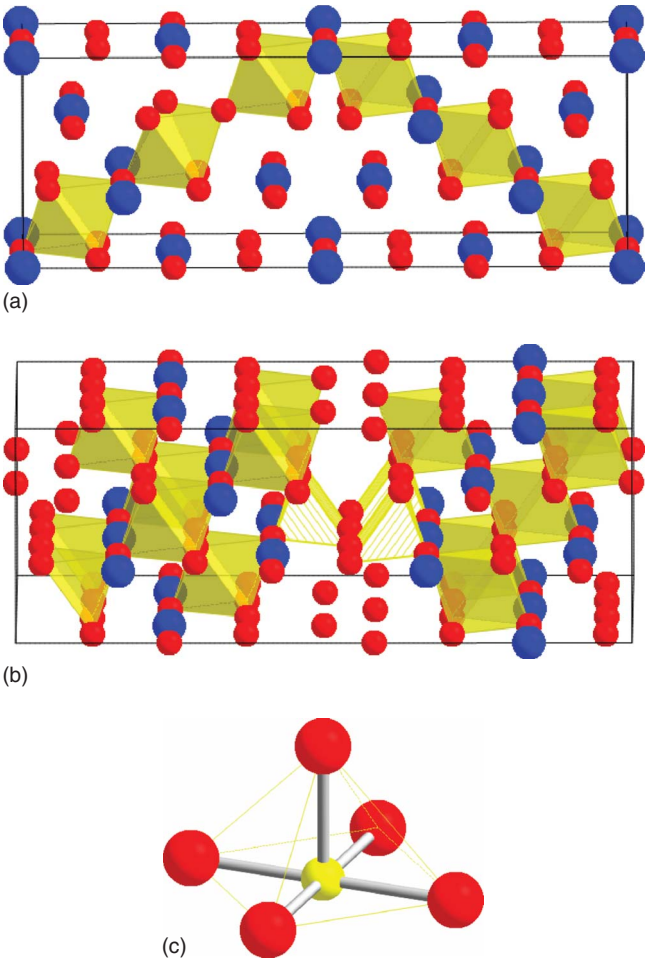

FIG. 8. (Color online) The two unrelaxed $\Sigma 3(112)$ grain boundaries with yellow Ti coordination polyhedra shown. The Ti ions are not shown, but they are located at the centers of the octahedra (or on the base of the square-based pyramids). The $\Sigma 3(112)(2/3,0)$ GB in (b) has been plotted as a $1\times 2\times 1$ supercell so the five-coordinate Ti atoms at the interface (enclosed in solid-stripe square-based pyramids) can be more easily seen. An individual five-coordinate Ti atom is shown in (c). The orientation of the boundaries is the same as in Figs. 2 and 3, except that the tilt axis is inclined to the page to reveal the coordination polyhedra more effectively.

The expansion for the $\Sigma 3(112)(2/3,0)$ boundary is also much larger (0.43 Å) than for the other boundaries however, puzzlingly, it has almost the same energy as the mirror symmetric $\Sigma 3(112)(0,0)$ GB (see Table III). Both CASTEP and the MBPP codes predict very similar results for these two boundaries, which gives us confidence that the observed similarities between the two interfaces are due to physical effects rather than numerical errors or inconsistencies. One might argue that there is no justification for our surprise at the two (112) GBs having such different expansions yet the same energy, given we have just stated that for boundaries with periodicity in the boundary plane, no simple relationship between energy and expansion exists. While this is true, one still intuitively expects that if the expansions between two boundaries differ by a significant amount, then their energies will also differ. Figure 8 shows the coordination envi-

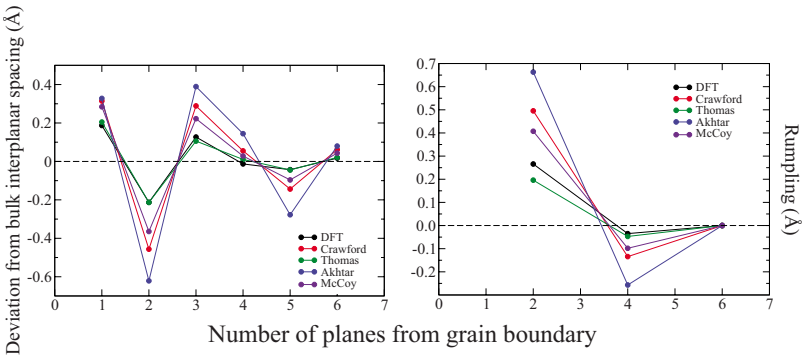

FIG. 9. (Color online) Left: Deviations from the bulk (111) interplanar spacing. Right: Variation in rumpling for a relaxed 120-atom model of a $\Sigma 3(111)$ grain boundary from both DFT-LDA and interatomic potential (frozen shells) calculations. The x axis represents the number of planes from the grain boundary for both graphs. The dashed lines at $y=0$ are a guide to the eye.

ronments of the Ti ions in each of the two boundaries. In bulk $SrTiO_3$, the Ti ions are surrounded by six O ions in an octahedral cage. This is also the case for the $\Sigma 3(112)(0,0)$ GB, where the Ti octahedra from each grain share corners at the grain boundary. In contrast, the Ti ions at the $\Sigma 3(112)(2/3,0)$ grain boundary are fivefold coordinated and form square-based pyramids, which also share corners across the boundary (this fivefold coordination of the Ti ions is particularly interesting because fivefold coordinate Ti is rarely found in naturally occurring solid-state materials). Exploring the effects of the differences in coordination of the Ti ions at the two grain boundaries may provide some clues about their structural and energetic properties. We are investigating this as part of a continuing study.

In the Sec. III B, we see how the candidate interatomic potentials perform in describing the structure and energetics of our chosen grain boundaries. Before moving on, let us summarize the results of the first-principles simulations:

(i) Two stable translation states were identified for the $\Sigma 3(112)$ boundaries, one at $\boldsymbol{t}=(0,0)$ and one at $\boldsymbol{t}=(2/3,0)$;

(ii) The $\Sigma 3(111)$ boundary has the lowest energy while the two (112) boundaries are indistinguishable in energy;

(iii) The $\Sigma 3(111)$ and $\Sigma 3(112)(0,0)$ boundaries have similar expansions while the $\Sigma 3(112)(2/3,0)$ GB has a much larger expansion;

(iv) All three boundaries exhibit interplanar spacing oscillations and rumpling of planes parallel to the boundary.

In order to be considered credible, an interatomic potential should be able to reproduce at least the structural trends. If it can also reproduce the DFT energy ordering of the boundaries, it would be considered very successful.

B. Interatomic potential calculations

The Akhtar, McCoy, and Crawford potentials consist of both short-range Buckingham and shell model terms. For these potentials we have performed calculations within the rigid ion model (Buckingham part only with "frozen" shells) and within the shell model. The results of the rigid ion model calculations are discussed first.

1. Rigid ion model calculations

Figure 9 compares the relaxed structure of the $\Sigma 3(111)$ boundary from both DFT-LDA and interatomic potential calculations. The Akhtar, McCoy, and Crawford potentials exaggerate both the interplanar spacing oscillations and rumpling compared to the DFT-LDA results. The Thomas potential, the simplest of the four we are testing, reproduces the DFT-LDA relaxation pattern quite well.

Figure 10 shows the interplanar spacing and rumpling oscillations for the relaxed $\Sigma 3(112)(0,0)$ boundary. This time there is less variation in how the interatomic potentials perform compared to the DFT-LDA structure and in contrast to the $\Sigma 3(111)$ GB, the potentials tend to slightly underestimate the atomic relaxations. DFT-LDA and potential calculations show relaxations that oscillate with the same phase and decay with distance from the interface in a similar way, although the amplitudes of the oscillations for the Akhtar potential are much greater and they decay more slowly.

The interplanar spacing and rumpling oscillations for the relaxed $\Sigma 3(112)(2/3,0)$ boundary are shown in Fig. 11. The potentials underestimate the deviation from the bulk interplanar spacing close to the boundary compared to DFT-LDA, but overestimate the magnitude of the rumpling. There is good agreement between the potentials and DFT-LDA as the distance from the boundary increases.

Table IV shows the energy and expansion for each boundary calculated with the four test potentials. None of the potentials is able to reproduce the energy ordering predicted by the DFT-LDA simulations. Both the Akhtar and Crawford

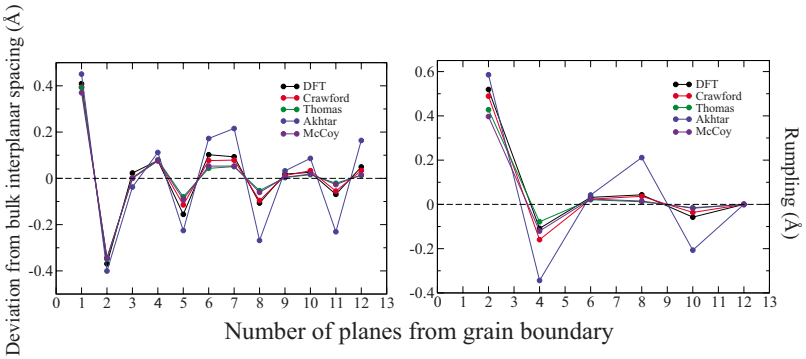

FIG. 10. (Color online) Left: Deviations from the bulk (112) interplanar spacing. Right: Variation in rumpling for a relaxed 120-atom model of a $\Sigma 3(112)(0,0)$ grain boundary from both DFT-LDA and interatomic potential (frozen shells) calculations. The x axis represents the number of planes from the grain boundary for both graphs. The dashed lines at $y=0$ are a guide to the eye.

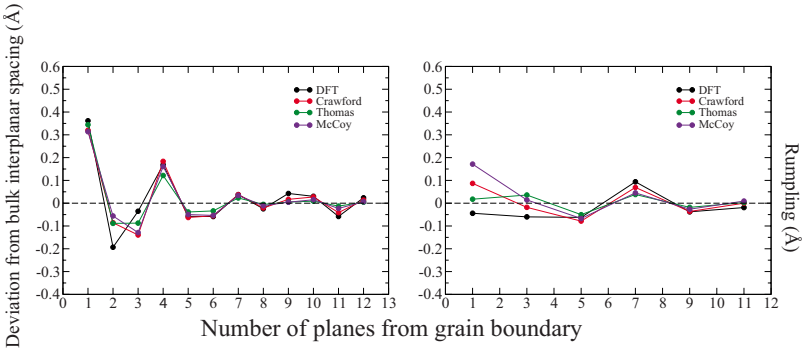

FIG. 11. (Color online) Left: Deviations from the bulk (112) interplanar spacing. Right: Variation in rumpling for a relaxed 120-atom model of a $\Sigma 3(112)(2/3,0)$ grain boundary from both DFT-LDA and interatomic potential (frozen shells) calculations. The x axis represents the number of planes from the grain boundary for both graphs. The dashed lines at $y=0$ are a guide to the eye.

potentials predict the $\Sigma 3(111)$ GB to be the highest in energy, whereas the *ab initio* simulations predict it to be the lowest in energy. The McCoy and Thomas potentials correctly give the $\Sigma 3(111)$ GB as the lowest energy but they both predict the $\Sigma 3(112)(2/3,0)$ to be lower in energy than the $\Sigma 3(112)(0,0)$ (these latter boundaries have almost the same energy in DFT-LDA calculations). Although the potentials perform poorly in predicting the energy trends between boundaries, they can reproduce the DFT-LDA trend for the expansions (with the exception of the Akhtar potential).

We have also studied the convergence behavior of the potentials by performing calculations on 60-, 120-, and 240-atom systems (the distance between the grain boundaries doubles as the number of atoms in the model doubles). The energies and expansions calculated with the Thomas and McCoy potentials for the two $\Sigma 3(112)$ boundaries are essentially converged with only 60 atoms. The energy and expansion calculated with the Crawford potential for the $\Sigma 3(112)(2/3,0)$ GB is converged with 60 atoms, however the energy and expansion for the $\Sigma 3(112)(0,0)$ interface do not appear to have converged with cell size.

All of the potentials show the same convergence behavior for the $\Sigma 3(111)$ GB: the expansion is smaller and the grain boundary energy is lower for the 60-atom model compared to the 120- and 240-atom models. This could be because there is an attractive interaction between the boundaries in the 60-atom model, the strength of which decreases as the distance between the boundaries in the 120- and 240-atom models increases. Another possibility is that the energy landscape for the 60-atom model contains a low-energy pathway to a structure with a smaller expansion and lower grain boundary energy (the energy landscape we are referring to is that of the "unconstrained γ surface," i.e., the atoms are freed to move in the x, y, and z directions). The 60-, 120-, and 240-atom models differ only in the amount of bulk material present between interfaces, however they all have different energy landscapes and the pathway to the minimum energy structure for the 60-atom model might be absent or difficult to get to in the 120- and 240-atom models. We tested these hypotheses by performing an additional set of calculations in which the 120-atom model was constructed by taking a relaxed 60-atom model and inserting the appropriate amount of unrelaxed bulk material between the boundaries. Any low-energy pathways might become more accessible if the grain boundary is deliberately prepared in a relaxed, low-energy state. We then performed a full relaxation on the "pre-relaxed" 120-atom boundary, calculating the expansion and energy as usual. The results obtained through this procedure were the same as those obtained through calculations on boundaries which had not been pre-relaxed. This suggests

TABLE IV. Relaxed grain boundary energies and expansions from interatomic potential calculations (rigid ion approximation).

Grain Boundary	Expansion (Å)	Energy (Jm^{-2})
McCoy		
$\Sigma 3(111)$, 60 atoms	0.17	0.59
120 atoms	0.24	0.81
240 atoms	0.24	0.86
$\Sigma 3(112)(0,0)$, 60 atoms	0.14	1.83
120 atoms	0.14	1.86
$\Sigma 3(112)(2/3,0)$, 60 atoms	0.43	1.47
120 atoms	0.43	1.46
Thomas		
$\Sigma 3(111)$, 60 atoms	0.15	0.29
120 atoms	0.17	0.35
240 atoms	0.17	0.35
$\Sigma 3(112)(0,0)$, 60 atoms	0.19	1.58
120 atoms	0.19	1.60
$\Sigma 3(112)(2/3,0)$, 60 atoms	0.48	1.26
120 atoms	0.48	1.26
Akhtar		
$\Sigma 3(111)$, 60 atoms	0.20	1.30
120 atoms	0.30	1.75
240 atoms	0.30	1.79
$\Sigma 3(112)(0,0)$, 60 atoms	0.17	1.11
120 atoms	0.14	1.10
$\Sigma 3(112)(2/3,0)$, 60 atoms	0.24	1.24
120 atoms	0.10	0.66
Crawford		
$\Sigma 3(111)$, 60 atoms	0.24	1.49
120 atoms	0.25	1.83
240 atoms	0.25	1.85
$\Sigma 3(112)(0,0)$, 60 atoms	0.17	1.67
120 atoms	0.19	1.76
240 atoms	0.14	1.64
$\Sigma 3(112)(2/3,0)$, 60 atoms	0.36	1.64
120 atoms	0.36	1.66

that attractive interactions between the boundaries in the 60-atom model are responsible for the smaller expansion and lower energy, rather than the absence of a low-energy pathway on the energy landscape for the 120- and 240-atom models.

Some general trends can be identified with respect to the grain boundary structures and energies produced by the interatomic potentials. The interplanar spacing and rumpling diagrams in Figs. 9–11 show that the agreement between the potentials and DFT-LDA generally improves as the distance from the boundary increases. This is not surprising considering the potentials have been fitted to the structure of bulk $SrTiO_3$. Of the (112) boundaries, the potentials predict the $\Sigma 3(112)(2/3,0)$ GB to be lower in energy by an amount greater (~25%) than that predicted by DFT-LDA (the Crawford potential gives the two boundaries as equal in energy; however, given the $\Sigma 3(111)$ GB is predicted to have the highest energy with this potential, the result is probably fortuitous). Both of these observations are linked to the transferability of the test potentials. The transferability of any potential is ultimately determined by the physics included in the form of the potential model. Hence, an improvement in the structural and energetic description of the grain boundaries would require going beyond the rigid ion approximation.

2. Shell model calculations

The interatomic potentials we have tested assume constant ionic charges on all the atoms in the system. Close to the interface however, the tendency for charge transfer from cation to anion will differ from that in the bulk.[33] Charge transfer is one way in which nearest-neighbor like-charged ions at the interface can reduce the electrostatic repulsion, so atoms close to the boundary may be more covalent than those in the bulk. Due to the lower point symmetry of the ions at interfaces, they can also lower their energy by dipole polarization. The rigid ion model is essentially a model of charged hard spheres and cannot describe these effects. Hence, if charge transfer and polarization effects are important close to interfaces (and in perovskite titanates, in general), then we might reasonably assume that a shell model will improve on the predictions of the rigid ion model. In fact, we found this not to be the case, as Fig. 12 illustrates. Figure 12 is an interplanar spacing diagram for the $\Sigma 3(111)$ GB calculated with the McCoy potential, in both its rigid ion and shell model variants; also shown are the DFT-LDA results. The shell model does not significantly improve on the rigid ion model structure and we found the same result for the Akhtar and Crawford potentials. There was also no or little improvement in the energy ordering of the boundaries. In addition, the shell model simulations became unstable in many cases. For example, if the core-shell displacements are too large, the core-shell distance can exceed the cutoff for the harmonic spring interaction (set at 0.6 Å in GULP). This results in shells detaching from their cores and attaching themselves to the cores of other ions. It is possible to avoid (or at least limit) this behavior by using an anharmonic spring constant. However, we felt this extra effort was not justified given that the shell model did not seem to improve the rigid ion results.

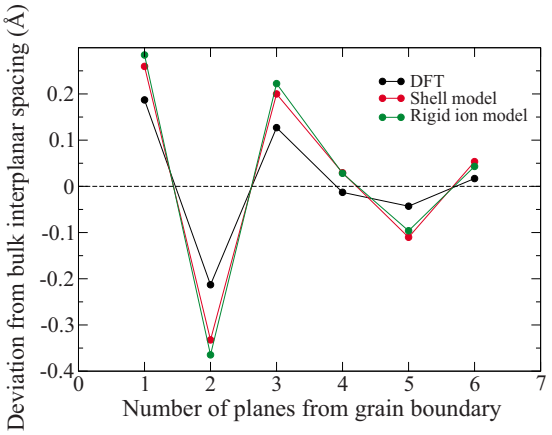

FIG. 12. (Color online) Deviations from the bulk (111) interplanar spacing for a relaxed 120-atom model of a $\Sigma 3(111)$ grain boundary from DFT-LDA and rigid ion and shell model calculations with the McCoy potential. The dashed line at $y=0$ is a guide to the eye.

We are not the first to note that shell models (in the form originally conceived by Dick and Overhauser) do not necessarily improve upon the rigid ion approximation.[26,35–37] Although our current findings suggest otherwise, we acknowledge that some authors have been able to successfully describe a range of phenomena using the shell model (in some cases it is difficult to credit the success of a calculation to the shell model because many authors do not test the rigid ion and shell model approximations separately). In a recent review, Phillpot and coworkers[38] cited several examples of shell models accurately reproducing the phase behavior of a number of complex oxides, including $KNbO_3$, $BaTiO_3$, and $PbTiO_3$. However, phase transitions in these materials proceed by symmetry lowering and this is easier to describe with a potential model than the complex polarization behavior of atoms at interfaces and grain boundaries. In previous work, we studied polarization effects at interfaces in the Ruddlesden-Popper and Magnéli phases of $SrTiO_3$ using a simplified tight-binding model and density functional perturbation theory (DFPT).[39] The tight-binding model was not able to describe the large enhancement of the Born effective charge for Ti at the Magnéli phase interface, even though it explicitly included intersite charge transfer interactions between the oxygen $2s$ and $2p$ and Ti $3d$ states. We can expect the Born effective charges of atoms at perovskite grain boundaries to be even more complex because the atoms are in very low symmetry environments. Hence, it is unlikely that a shell model will be able to capture the essential physics required to reproduce the Born effective charge of an O or Ti atom at a grain boundary in $SrTiO_3$.[40]

C. Grain boundary structures from interatomic potential calculations

Table IV shows that the Thomas, McCoy, and Crawford potentials predict the correct trend for the expansion of the

TABLE V. Grain boundary energies of interatomic potential structures calculated with DFT-LDA.

	Energy (Jm^{-2})		
Model	$\Sigma3(111)$	$\Sigma3(112)(0,0)$	$\Sigma3(112)(2/3,0)$
McCoy	1.29	1.29	1.81
Akhtar	1.50	1.43	1.93
Thomas	0.81	1.16	1.37
Crawford	1.11	1.17	1.56
DFT-LDA	0.53	1.06	1.06

boundaries. Although there are some discrepancies between the structures produced by the potentials and the DFT-LDA structures, Figs. 9–11 show that there is generally reasonable agreement between them. One way to quantify the quality of the interatomic potential structures is to take their coordinates and perform a single-point DFT energy calculation, i.e., no further atomic relaxation. If the interatomic potential structures are really in good agreement with the DFT-LDA structures, their energies should be closely clustered just above the DFT-LDA energies. We performed this additional series of calculations for all four of our test potentials; the results are shown in Table V.

Given the results presented in Table IV, we might expect the energies of the Thomas and McCoy structures to be closest to the DFT-LDA energies, followed by the Crawford and Akhtar structures. Table V shows that the Akhtar potential does indeed produce the worst quality structures but the trends for the other potentials are somewhat unexpected. The McCoy structures for the $\Sigma3(111)$ and $\Sigma3(112)(0,0)$ boundaries are predicted by DFT-LDA to be equal in energy, whereas the McCoy potential predicts the $\Sigma3(111)$ GB to be the lowest in energy (see Table IV). Conversely, the Crawford structure for the $\Sigma3(111)$ GB is predicted by DFT-LDA to be the lowest in energy of the three boundaries, whereas the Crawford potential predicts the same boundary to be the highest in energy. The Thomas structures are closest in energy to the DFT-LDA ones. None of the potentials produce structures for the two $\Sigma3(112)$ boundaries which are indistinguishable in energy (like the DFT-LDA structures). However, Table IV shows that the Thomas and McCoy potentials both predict the $\Sigma3(112)(2/3,0)$ boundary to be lower in energy than the $\Sigma3(112)(0,0)$ GB, whereas Table V shows the opposite trend: DFT-LDA predicts the McCoy, Thomas, and Crawford $\Sigma3(112)(2/3,0)$ structures to be higher in energy than the $\Sigma3(112)(0,0)$ GB structures. Figure 11, the interplanar spacing and rumpling diagram for the $\Sigma3(112)(2/3,0)$ GB, shows that all of the potentials overestimate the magnitude of the rumpling close to the interface. The McCoy potential overestimates the most, followed by the Crawford potential, while the Thomas potential overestimates the least. Looking at Table V, the energy of the $\Sigma3(112)(2/3,0)$ GB produced by the McCoy potential deviates the most from the DFT-LDA result, followed by the Crawford structure. The energy of the $\Sigma3(112)(2/3,0)$ GB produced by the Thomas potential is closest to the DFT-LDA energy. This suggests that, for the $\Sigma3(112)(2/3,0)$ GB at least, the potentials favor structures with greater rumpling at the interface.

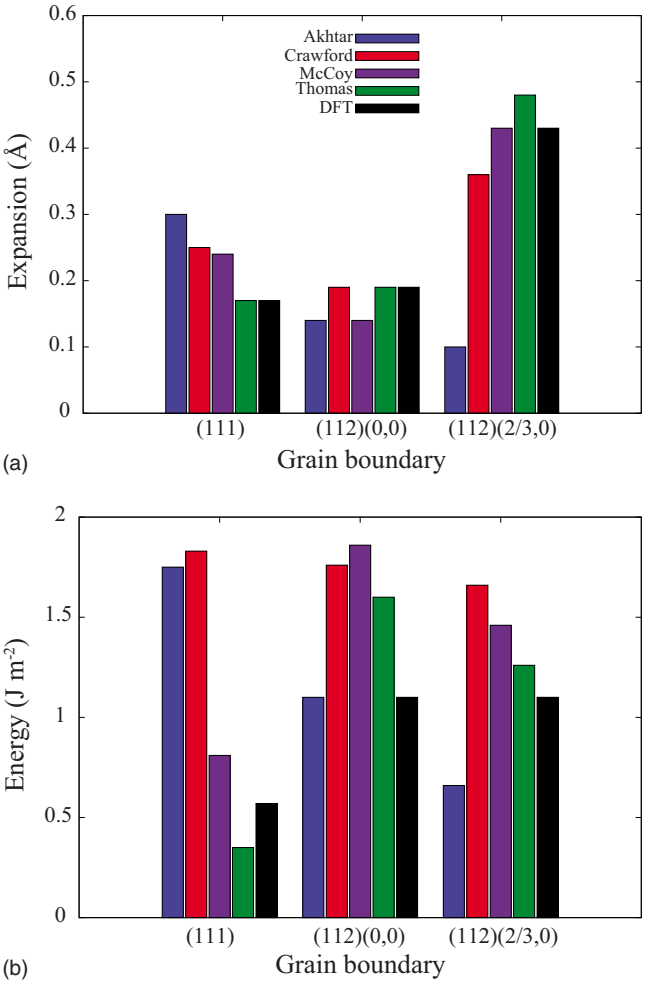

FIG. 13. (Color online) Comparison of interatomic potential results and DFT-LDA for the boundary expansion (top) and boundary energy (bottom) for all three interfaces. The color key is the same for both graphs.

The results of our interatomic potential calculations can be summarized as follows:

(i) None of the potentials can accurately predict the correct energy ordering of the boundaries, although the Thomas and McCoy potentials do give the $\Sigma3(111)$ as the lowest energy;

(ii) The Thomas, McCoy, and Crawford potentials predict the correct trend for the expansion and the Thomas potential produces structures in reasonable agreement with DFT-LDA;

(iii) The shell model does not improve upon the rigid ion approximation for the potentials we have tested.

These points are summarized graphically in Fig. 13.

IV. DISCUSSION

There have been far fewer classical (or *ab initio*) simulation studies on grain boundaries in ionic oxides than in metals however, there are some examples in the literature. How do our findings compare to those of other authors?

Tasker and Duffy[35] studied the structure of a $\Sigma5(001)$ twist boundary in NiO using a rigid ion model (they also tried a shell model but concluded that it did not change the results significantly). Their simulations predicted a structure with a small expansion and a reduced density of ions in the boundary plane. The results are consistent with the experimental observations of Sun and Balluffi[41] on the stability of twist boundaries in another rocksalt-structured oxide, MgO. Shell model calculations on the same $\Sigma5[001]$ twist boundary in MgO also showed that the boundary was stable only if ions were removed from the boundary plane.[42] The structure produced by the shell model calculations was later confirmed by DFT simulations.[43]

Shell model calculations on the $\Sigma5(\bar{1}20)[001]$ tilt boundary in TiO_2 predicted a stable structure characterized by an in-plane translation of $(1/6)a_0[\bar{1}20]$ (the authors do not give the reference state from which the translation is measured).[44] Image simulations on the theoretical structure were in good agreement with experimental HRTEM images, although the shell model did not reproduce the negative expansion (contraction) observed experimentally. DFT calculations on the same interface also failed to predict a contraction of the boundary but did confirm the translation state as $(1/6)a_0[\bar{1}20]$.[45]

Marinopoulos *et al.*[46] carried out a series of DFT and shell model calculations in an effort to determine the most stable basal twin interface in α-Al_2O_3. Their DFT results indicated that the rotation twin was the most energetically favorable, consistent with HRTEM experiments. The structures produced by the shell model were in reasonable agreement with the DFT structures; however, the shell model was unable to reproduce the magnitude of the energy differences between the candidate structures or the DFT energy ordering for the two higher-energy twin boundaries.

Finally, there have been a few previous atomistic simulation studies on grain boundaries in $SrTiO_3$. Kienzle and coworkers[47] calculated the structure and energy of the SrO- and Ti-terminated $\Sigma3(111)$ GBs using the shell model of Akhtar. The Ti-terminated variant was correctly predicted to be lower in energy than the SrO-terminated GB [compared to DFT (Ref. 11)], although the authors also noted that there were significant discrepancies between the experimental structure and those produced by the shell models. Ravikumar *et al.*[48] studied the structure and energetics of the $\Sigma5(310)[001]$ tilt boundary in $SrTiO_3$ using the Akhtar potential with frozen shells. The theoretical results were compared to *Z*-contrast scanning transmission electron microscopy (STEM) images[49] of the same boundary. The authors concluded that although some basic structural trends were common to both the experimental and theoretical results, quantitative comparisons would require both approaches to be "refined considerably."[49]

It is difficult to draw systematic conclusions from the studies reviewed above because the methods used in each case are slightly different. Some authors have performed interatomic potential calculations on the structure of a given boundary and compared the result to experiment. Some authors have compared experimental results to both interatomic potential and DFT calculations. Most authors have considered only a single boundary and all authors have used a single interatomic potential. Systematic studies on the reliability of classical potentials for grain boundaries in ionic oxides are lacking. Nonetheless, some general trends seem to emerge. Structures produced by interatomic potential calculations agree reasonably well with experiment and, where the data is available, structures produced by DFT calculations. The potentials do less well in correctly ordering the energies of boundaries, or predicting energy differences between boundaries. Despite this latter inadequacy, in all the cases discussed above, results from interatomic potential calculations have aided the interpretation of experimental data and, in combination with DFT calculations, provided qualitative insights which would not be accessible from an experimental analysis alone.

V. SUMMARY AND CONCLUSIONS

We have calculated the relaxed structures and energies of the $\Sigma3(111)$, $\Sigma3(112)(0,0)$, and $\Sigma3(112)(2/3,0)$ grain boundaries in $SrTiO_3$ with four different interatomic potentials; the results were compared to DFT-LDA calculations on the same boundaries. Our aim was to identify a potential which could accurately describe at least the structures of our chosen grain boundaries (compared to DFT-LDA) and which could therefore be used in larger-scale atomistic simulations of more complex $SrTiO_3$ interfaces. We have also critically examined the shell model approximation.

None of the interatomic potentials we tested produced grain boundary energy orderings in agreement with the DFT-LDA calculations. The Thomas and McCoy potentials correctly predict the $\Sigma3(111)$ GB to be the lowest in energy but are not transferable enough to reproduce the DFT-LDA energy ordering of the two $\Sigma3(112)$ boundaries. This is probably due to the presence of fivefold coordinate Ti ions at the $\Sigma3(112)(2/3,0)$ interface, i.e., the fivefold coordinate Ti ions are chemically different to the sixfold coordinate Ti ions at the $\Sigma3(112)$ interface and the rigid ion model cannot capture these differences. Both the Crawford and Akhtar potentials predict the $\Sigma3(111)$ GB to be the highest in energy.

All the potentials (with the exception of the Akhtar potential) produce structures which are in reasonably good agreement with those from DFT-LDA calculations. The structures generated by the Thomas potential are closest in energy to the DFT-LDA structures. The agreement between DFT-LDA and the Thomas and McCoy potentials with respect to grain boundary expansions is particularly impressive considering the simplicity of the rigid ion model. The agreement between the potentials and DFT-LDA generally improves as the distance from the boundary increases, i.e., as the atomic structure tends to that of bulk $SrTiO_3$. Close to the boundary, the potentials struggle to describe the structural distortions caused by large interplanar spacing and rumpling oscillations.

Our attempts to improve upon the rigid ion results by performing an additional series of shell model calculations were not successful. We found that the grain boundary energies and structures calculated with the shell models we tested differed little from the rigid ion model results. We argue that

this simple model of dipolar polarizability will be unable to (routinely) correctly describe the complex polarization behavior found at $SrTiO_3$ interfaces and grain boundaries, where the atoms are in low-symmetry environments.

We considered only stoichiometric grain boundaries in this work but in a "real" $SrTiO_3$ polycrystal, which will contain dopants, defects, and impurities, the vast majority of boundaries are likely to be nonstoichiometric. Hence, it is worth considering how our conclusions might be modified if the potentials were tested on nonstoichiometric interfaces. As noted in Sec. I, the energy of nonstoichiometric grain boundaries is a function of the chemical potentials of the component materials. For $SrTiO_3$ we might choose those components to be SrO, TiO_2, and O. The chemical potentials of these compounds in their standard states can be approximated as the total energies of bulk SrO and TiO_2 at $T=0$ K (a thermodynamic cycle can be constructed to calculate the chemical potential of oxygen, as described in Ref. 50). However, we cannot get much further with interatomic potentials. The total energies of these bulk quantities must be calculated using the Sr-O and Ti-O interaction potentials from the *same* $SrTiO_3$ interatomic potential used to calculate the grain boundary total energy. This will induce an error in the computed interfacial energy because the individual interaction potentials will not be sufficiently transferable. Charge transfer and charge density rearrangement effects will be greater if there are point defects and dopants at the interface and the potentials would have to describe the energies of the relevant point defects. Furthermore, since nonstoichiometry introduces the possibility of charged defects, the electronic structure must be explicitly considered. The energy of charged point defects depends on the Fermi energy, which in turn depends on the doping or stoichiometry. Hence, the rigid ion approximation will become increasingly more severe and increasingly less accurate. It is unlikely that any of the potentials we have tested are transferable enough to accurately describe nonstoichiometric grain boundaries. The performance of the potentials discussed above should therefore probably be regarded as the "best case scenario."

ACKNOWLEDGMENTS

Financial support for this work was provided by the European Commission under Contract No. Nr. NMP3-CT-2005-013862 (INCEMS). The calculations were performed using the facilities of the High Performance Computing Service at Imperial College London and the Scientific Supercomputing Centre at the University of Karlsruhe (SSCK). We also acknowledge the support of the HPC-Europa program.

*n.benedek@imperial.ac.uk

[1] A. P. Sutton and V. Vitek, Philos. Trans. R. Soc. London, Ser. A **309**, 1 (1983).
[2] H. Van Swygenhoven, P. M. Derlet, and A. G. Froseth, Nat. Mater. **3**, 399 (2004).
[3] S. von Alfthan, K. Kaski, and A. P. Sutton, Phys. Rev. B **76**, 245317 (2007).
[4] K. Szot, W. Speier, G. Bihlmayer, and R. Waser, Nat. Mater. **5**, 312 (2006).
[5] H. Ohta, Mater. Today **10**, 44 (2007).
[6] V. Vitek, Philos. Mag. **18**, 773 (1968).
[7] O. Kienzle and F. Ernst, J. Am. Ceram. Soc. **80**, 1639 (1997).
[8] Z. Zhang, W. Sigle, F. Phillipp, and M. Rühle, Science **302**, 846 (2003).
[9] S. Hutt, S. Köstlmeier, and C. Elsässer, J. Phys.: Condens. Matter **13**, 3949 (2001).
[10] R. Astala and P. D. Bristowe, J. Phys.: Condens. Matter **14**, 6455 (2002).
[11] S. Gemming and M. Schreiber, Chem. Phys. **309**, 3 (2005).
[12] S. Hutt, O. Kienzle, F. Ernst, and M. Rühle, Z. Metallkd. **92**, 105 (2001).
[13] D. Alfé and M. J. Gillan, J. Phys. Condens. Matter **18**, L435 (2006).
[14] V. N. Staroverov, G. E. Scuseria, J. Tao, and J. P. Perdew, Phys. Rev. B **69**, 075102 (2004).
[15] J. P. Perdew, A. Ruzsinszky, G. I. Csonka, O. A. Vydrov, G. E. Scuseria, L. A. Constantin, X. Zhou, and K. Burke, Phys. Rev. Lett. **100**, 136406 (2008).
[16] Y. Zhao and D. G. Truhlar, J. Chem. Phys. **128**, 184109 (2008).
[17] B. G. Dick and A. W. Overhauser, Phys. Rev. **112**, 90 (1958).
[18] C. R. A. Catlow, I. D. Faux, and M. J. Norgett, J. Phys. C **9**, 419 (1976).
[19] N. C. Pyper, J. Chem. Phys. **114**, 4390 (2001).
[20] N. A. Marks, M. W. Finnis, J. H. Harding, and N. C. Pyper, J. Chem. Phys. **114**, 4406 (2001).
[21] A. J. Rowley, P. Jemmer, M. Wilson, and P. A. Madden, J. Chem. Phys. **108**, 10209 (1998).
[22] M. W. Finnis, *Interatomic Forces in Condensed Matter* (Oxford University Press, New York, 2003).
[23] M. J. Akhtar, Z. Akhtar, R. A. Jackson, and C. R. A. Catlow, J. Am. Ceram. Soc. **78**, 421 (1995).
[24] M. A. McCoy, R. W. Grimes, and W. E. Lee, Philos. Mag. A **75**, 833 (1997).
[25] J. Crawford and P. Jacobs, J. Solid State Chem. **144**, 423 (1999).
[26] B. S. Thomas, N. A. Marks, and B. D. Begg, Nucl. Instrum. Methods Phys. Res. B **228**, 288 (2005).
[27] J. D. Gale and A. L. Rohl, Mol. Simul. **29**, 291 (2003).
[28] S. J. Clark, M. D. Segall, C. J. Pickard, P. J. Hasnip, M. J. Probert, K. Refson, and M. C. Payne, Z. Kristallogr. **220**, 567 (2005).
[29] B. Meyer, C. Elsässer, M. Lechermann, and M. Fähnle, FORTRAN90 program for mixed-basis pseudopotential calculations for crystals.
[30] C. Elsässer, T. Takeuchi, K. M. Ho, C. T. Chan, P. Braun, and M. Fähnle, J. Phys.: Condens. Matter **2**, 4371 (1990).
[31] T. Ochs and C. Elsässer, Z. Metallkd. **93**, 406 (2002).
[32] B. Meyer, J. Padilla, and D. Vanderbilt, Faraday Discuss. **114**, 395 (1999).
[33] A. P. Sutton and R. W. Balluffi, *Interfaces in Crystalline Materials* (Oxford University Press, New York, 1996).

[34] A. P. Sutton, Philos. Mag. A **63**, 793 (1991).
[35] P. W. Tasker and D. M. Duffy, Philos. Mag. A **47**, L45 (1983).
[36] D. R. Collins and W. Smith, Council for the Central Laboratories of the Research Councils Technical Report No. DL-TR-96-001, 1996.
[37] A. Aguado, L. Bernasconi, and P. A. Madden, Chem. Phys. Lett. **356**, 437 (2002).
[38] S. R. Phillpot, S. B. Sinnott, and A. Asthagiri, Annu. Rev. Mater. Res. **37**, 239 (2007).
[39] N. A. Benedek, C. Elsässer, and M. W. Finnis, J. Phys.: Conf. Ser. **94**, 012005 (2008).
[40] We could find very few studies in the literature on the performance of the shell model in calculating Born effective charge tensors. One particularly impressive example is provided by the work of Gale and Rohl (Ref. 27), who calculated the Born effective charges (BEC) for α quartz using a Buckingham potential in combination with the shell model. There was excellent agreement between the Born effective charges calculated with the interatomic potential and those from an earlier DFT-LDA calculation. BECs have also been calculated with an interatomic potential for bulk $BaTiO_3$; there was reasonable agreement with experiment and DFT (Ref. 51). As far as we are aware, there exist no systematic studies on the performance of interatomic potentials for dynamical properties of titanate perovskites.
[41] C. P. Sun and R. W. Balluffi, Philos. Mag. A **46**, 49 (1982).
[42] D. C. Sayle, T. X. T. Sayle, S. C. Parker, J. H. Harding, and C. R. A. Catlow, Surf. Sci. **334**, 170 (1995).
[43] J. H. Harding and C. Noguera, Philos. Mag. Lett. **77**, 315 (1998).
[44] W. Y. Lee, P. D. Bristowe, I. G. Solozarno, and J. B. Vandersande, *Defect-Interface Interactions* (Materials Research Society, Pittsburgh, 1994).
[45] I. Dawson, P. D. Bristowe, M. H. Lee, M. C. Payne, M. D. Segall, and J. A. White, Phys. Rev. B **54**, 13727 (1996).
[46] A. G. Marinopoulos, S. Nufer, and C. Elsässer, Phys. Rev. B **63**, 165112 (2001).
[47] O. Kienzle, M. Exner, and F. Ernst, Phys. Status Solidi A **166**, 57 (1998).
[48] V. Ravikumar, V. P. Dravid, and D. Wolf, Interface Sci. **8**, 157 (2000).
[49] V. P. Dravid and V. Ravikumar, Interface Sci. **8**, 177 (2000).
[50] M. W. Finnis, A. Y. Lozovoi, and A. Alavi, Annu. Rev. Mater. Res. **35**, 167 (2005).
[51] M. Sepliarsky, M. G. Stachiotti, and S. R. Phillpot, in *Handbook of Materials Modeling*, edited by S. Yip (Springer, New York, 2005).